Progress in Natural Science: Materials International 36 (2026) 94–101

HOSTED BY

Contents lists available at ScienceDirect

Progress in Natural Science: Materials International

journal homepage: www.elsevier.com/locate/pnsmi

The synergy of Fe and Mn as layered double hydroxides for electrochemical arsenic remediation

Song Peng[a], Tiantian Wang[a], Yang Wang[a, b, c, *]

[a] School of Chemical Engineering and Technology, Tianjin University, Tianjin, 300350, China
[b] Tianjin Key Laboratory of Membrane Science and Desalination Technology, Tianjin, 300072, China
[c] National Industry-Education Integration Platform of Energy Storage, Tianjin University, Tianjin, 300350, China

ARTICLE INFO

Keywords:
Layered double hydroxides
Electrochemical arsenic remediation
Hydrothermal
Coprecipitation

ABSTRACT

Arsenic pollution in water poses a significant environmental challenge due to its high toxicity and non-degradability. In this study, FeMn-layered double hydroxide (FeMn-LDH) was synthesized using hydrothermal and coprecipitation methods with different precursors for electrochemical arsenic remediation. The crystallinity of FeMn-LDH was enhanced with nitrate precursor compared to chloride precursor. The corresponding calcined layered double oxide obtained through the coprecipitation method (FMO-NO_3-Co) exhibits a significantly increased specific surface area and an optimal average pore size, facilitating efficient ion transport, and enhanced oxidation state of Mn, increasing arsenic removal efficiency. Electrochemical tests indicate that FMH-NO_3-Co exhibits relatively high specific capacitance and excellent electrochemical performance. Notably, the FMO-NO_3-Co achieves an electrosorption capacity of 55.5 mg g^{-1} with 56.6 % of As(III) being electrochemically oxidized, demonstrating superior electrocatalytic activity for the oxidation of As(III) and high-performance electrosorption of As(V). The arsenic removal mechanism was comprehensively analyzed, revealing that Mn^{2+}/Mn^{3+} redox cycling played a key role in As(III) oxidation, while Fe-based coordination sites contributed to As(V) adsorption. Furthermore, the enhanced porosity and conductivity of the calcined LDH materials significantly improved charge transfer efficiency, thereby accelerating the arsenic removal process. Overall, this study provides valuable insights into the potential application of FeMn-LDH in electrochemical arsenic remediation.

1. Introduction

In the context of escalating environmental challenges, the issue of arsenic pollution in water has emerged as a critical concern [1,2]. Since arsenic cannot be naturally degraded by chemical and biological processes, it easily accumulates in the food chain with biogeochemical cycling, and thereby harming both ecosystems and human health [3]. Long-term excessive consumption of water with excessive arsenic content can lead to cardiovascular diseases, chronic poisoning, acute poisoning, and even cause symptoms such as carcinogenesis, teratogenesis, and mutagenesis [4,5]. Arsenic exists in various forms in water and is mainly divided into arsenite (trivalent arsenic, As(III)) and arsenate (pentavalent arsenic, As(V)), with different oxidation states exhibiting distinct chemical behaviors and toxicity levels [6,7]. The removal of As(III) has proven to be particularly challenging due to its relatively high mobility and toxicity compared to other forms [8].

With the continuous expansion of industrial activities and the increasing demand for water resources, the need for efficient arsenic removal methods has become extremely urgent. Traditional arsenic removal techniques such as precipitation [9], adsorption [10], coagulation [11], and ion exchange [12] often face limitations in terms of efficiency, cost, and potential secondary pollution. Capacitive deionization (CDI), or Electrochemical Ion Separation (EIONS), in particular, has emerged as an attractive option. CDI operates by using highly porous electrodes in a low potential electric field to remove ions from water through electrosorption [13]. It offers advantages like low energy consumption, easy electrode regeneration, and minimal environmental impact [14]. Membrane CDI (MCDI) in particular is characterized by the integration of ion exchange membranes that can alleviate the problem of co-ion expulsion, thereby increasing the efficiency and effectiveness of ion separation. CDI has been applied to brackish water desalination [15], hard water softening [16], heavy metal removal [17], groundwater

This article is part of a special issue entitled: Environ. Funct. Mater. published in Progress in Natural Science: Materials International.

* Corresponding author. School of Chemical Engineering and Technology, Tianjin University, Tianjin, 300350, China.
E-mail address: yangwang2017@tju.edu.cn (Y. Wang).

https://doi.org/10.1016/j.pnsc.2025.11.010
Received 22 April 2025; Received in revised form 21 November 2025; Accepted 25 November 2025
Available online 31 January 2026

remediation [18], nutrient recovery [19] and wastewater recycling [20].

Currently, electrode materials are considered to be the most significant influencing factor in the CDI system. It has been demonstrated that CDI process can remove arsenic with the oxidation of As(III) and adsorption of As(V) using metal oxide and activated carbon electrodes in a potential of 1.0–1.4 V. For example, in an activated carbon-based CDI, the removal of neutral As(III) can be achieved by the in-situ oxidation of As(III) to As(V) at 1.2 V, followed by the electrosorption of negatively-charged As(V) onto the anode syrface [21]. However, the development of this technique could be restricted by the low conversion of As(III) to As(V) during the charging step. Manganese (Mn) is a redox-active metal and the higher valence state of Mn plays a crucial role in the oxidation of As due to its favorable redox potential [22–24]. In addition, Fe and Fe oxide are found to be effective adsorbents due to their high affinity for removal against arsenic [25–27]. A typical example of the application of Mn-Fe bimetallic oxides for arsenic removal is the utilization of the standard redox potential difference and synergistic effect of different valence states of Fe and Mn in nanosized magnetic mesoporous iron manganese bimetal oxides by Wen et al. [28]. In this case, the surface-bound Fe(II) was associated with $\cdot OH_{ads}$ radicals generated by the Fenton-like pathway. $\cdot OH_{free}$ radicals (30.39 %) and surface-adsorbed $\cdot OH_{ads}$ radicals (69.16 %) oxidized As(III) to As (V), which were adsorbed on the surface, thus realizing arsenic conversion and absorption.

Layered double hydroxide (LDHs) is a commonly used electrode material in CDI system [29–32], possess considerable electrochemical capacity [33] and have demonstrated significant potential in the energy storage [34,35]. A notable example is the nano-onion-like NiCoMn-LDHs developed by Zhang et al. [36], which achieved a specific capacitance as high as 4413 F g^{-1} at a current density of 1 A g^{-1}. Consequently, their potential for arsenic removal has also been actively explored. For instance, some studies have explored the use of ZnAl-LDH and MgAl-LDH in adsorbing arsenic species. In this study, FeMn-LDHs will be designed with unique advantages for the effective removal of arsenic from water. Mn can exist in multiple oxidation states and is capable of facilitating the oxidation of As(III) to the less toxic and more easily removable As(V), while Fe can interact with arsenic through coordination bonds, enhancing the adsorption capacity. We aim to conduct a systematic investigation of their synthesis methods, the morphological, structural, and chemical properties, and the performance in electrochemical and adsorption processes associated with arsenic removal. Most importantly, the coupling electrocatalytic oxidation and electrosorption reactions in arsenic removal will be carefully exhibited. We hope to provide a more efficient and sustainable solution to the problem of arsenic contamination in water sources.

2. Experimental

2.1. Materials

$FeCl_3{\cdot}6H_2O$ (99 %), $Fe(NO_3)_3{\cdot}9H2O$ (99 %), $MnCl_2{\cdot}4H_2O$ (99 %), $Mn(NO_3)_2{\cdot}9H_2O$ (99 %), $CO(NH_2)_2$ (99 %), NH_4F (99 %), and N-Methyl-2-pyrrolidone (NMP, 99 %) were purchased from Shanghai Macklin Biochemical Co., Ltd. Sodium hydroxide (NaOH, 99 %) and anhydrous sodium carbonate (Na_2CO_3, 99 %) were purchased from Tianjin Jiangtian Chemical Co., Ltd. Polyvinylidene fluoride (PVDF, 99 %) was purchased from Alfa Aesar Chemical Co., Ltd.

2.2. Synthesis of FeMn-LDH/LDO electrodes

FeMn-LDHs were synthesized using the typical hydrothermal method and co-precipitation method, respectively. In the hydrothermal method, initially, $FeCl_3{\cdot}6H_2O$ (5 mmol) and $MnCl_2{\cdot}4H_2O$ (2.5 mmol), were mixed in 60 mL water followed by the addition of urea (10 mmol) and NH_4F (4 mmol) with constant stirring for 30 min to obtain a homogeneous solution. The prepared solution was transferred to a PTFE-lined autoclave with a volume of 100 mL and slowly heated up from room temperature to 120 °C in a muffle furnace and kept for 12 h, and subsequently cooled to room temperature. Lastly, the reaction products were rinsed with anhydrous ethanol and deionized water alternately and dried in a vacuum oven at 60 °C for 12 h. The obtained products were marked as FMH-Cl-Hy. Replace the metal chlorides with an equivalent amount of metal nitrates while maintaining other conditions unchanged. The obtained products were marked as FMH-NO_3-Hy.

In the synthesis by coprecipitation method, $FeCl_3{\cdot}6H_2O$ (10 mmol) and $MnCl_2{\cdot}4H_2O$ (10 mmol) were dispersed into 100 mL of deionized water and stirred at a constant speed for 30 min to form solution A. Solution B was formed by dissolving NaOH (35 mmol) and Na_2CO_3 (15 mmol) in 100 mL of deionized water. Additionally, buffer solution C with a pH of approximately 10 was prepared by adding 5 mg of Na_2CO_3 to 50 mL deionized water. Then, solution A and solution B were dripped slowly into solution C and the pH value of the resulting suspension was strictly adjusted to 10.4–10.7. The mixture was ultrasonic processed at room temperature for 30 min and then stirred in a water bath at 70 °C for 6 h. Lastly, the reaction products were rinsed with anhydrous ethanol and deionized water alternately and dried in a vacuum drying oven at 60 °C for 12 h. The obtained products were marked as FMH-Cl-Co. Replace the metal chlorides with an equivalent amount of metal nitrates while maintaining other conditions unchanged. The obtained products were marked as FMH-NO_3-Co.

During the experimental investigation, FMH-NO_3-Co demonstrated superior performance among the four synthesized LDH materials. This particular LDH was subjected to a calcination process transforming LDH into a layered double oxide (LDO). The FMH-NO_3-Co was placed in a tube furnace and calcined at a temperature of 400 °C for a duration of 2 h. The resulting material was named as FMO-NO_3-Co. This calcination treatment is expected to induce structural and chemical changes in the material, especially for enhancing the valence state of Mn. The elevation of the valence state might play a crucial role in the oxidation of As(III).

The FeMn-LDH electrode was prepared by coating an active materials layer on a current collector. First, 160 mg of FeMn-LDH, 20 mg of carbon black and 20 mg PVDF were added to 950 μL NMP solution. Through stirring for 12 h, the homogeneous dispersion was coated on the graphite paper or titanium sheet. After drying, the electrode had a total mass load of 2–3 mg cm^{-2}. The activated carbon (AC) electrode was prepared according to the same protocol.

2.3. Materials characterizations

X-ray diffraction (XRD, D8-Focus) was used to determine the crystal structure of the sample at 5° min^{-1} using Cu Kα radiation (λ = 0.15406 nm), and the operating voltage was 49 kV. A field emission scanning electron microscope (SEM, Regulus 8100) and transmission electron microscope (TEM, JEM-2100F) with an energy-dispersive X-ray spectrometer were used to analyze the morphology of the samples. The chemical state was analyzed by X-ray photoelectron spectroscopy (XPS, Thermo ESCALAB 250Xi) with an Al Kα (1486.6 eV) X-ray source. The N_2 adsorption-desorption isotherms were performed with Quantachrome AUTOSORB IQ at 77.3 K. The specific surface area (SSA) was calculated based on the N_2 adsorption-desorption isotherm via the BET method, and the pore size distribution was derived from the Barrett-Joyner-Halenda method. The ion concentration was detected by an inductively coupled plasma-optical emission spectrometer (ICP-OES, 5100 series, Agilent Technologies, USA).

2.4. Measurements

The electrochemical characteristics of the FeMn-LDH electrodes (2 cm × 2 cm) were studied in a three-electrode system employing an electrochemical workstation (Bio-Logic VSP). Ag/AgCl(E^0 = 0.197 V), and Platinum mesh were used as the reference electrode and counter electrode, respectively. Cyclic voltammetry (CV, 5 mV s^{-1} and −1.0–1.0 V) and galvanostatic charge-discharge (GCD, 0–0.4 V, 1 A g^{-1})

were performed in the 1 mol L^{-1} Na_2SO_4 solution. The electrochemical impedance spectroscopy (EIS) test was conducted in the frequency range of 0.01–100 kHz at a potential of 0.7 V versus RHE.

The adsorption experiments were carried out in a two-electrode configuration consisting of a FeMn-LDH working electrode (4 cm × 4 cm) and an AC counter electrode, which was used to absorb cations in the electrical double layer. During the adsorption and desorption, a constant cell voltage (1.2 V and −1.2 V, respectively) was applied for 90 min. The selective sorption and conversion of As(III) into As(V) were investigated in the FMO-NO_3-Co/AC cell containing 50 mL of 2 mM $NaAsO_2$, 10 mM NaCl, and 10 mM $NaHCO_3$ in a bath mode. The arsenic sorption capacity (τ, mg As g^{-1}) and removal efficiency (R, %) were calculated by the following equations:

$$\tau = \frac{(C_0 - C_f)V}{m} \quad (1)$$

$$R = \left(\frac{1 - C_f}{C_0}\right) \times 100 \quad (2)$$

where C_0 is the initial concentration of arsenic, C_f is the final concentration after electrosorption, V is the volume of the solution, m is the mass of the working electrode, and R is the removal efficiency of As.

3. Results and discussions

The surface morphology and crystallography of the as-prepared LDHs were performed by SEM and TEM in Fig. 1. The sizes of all the synthesized particles were about several hundred nanometers as irregular or chaotic structures except FMH-Cl/NO_3-Hy. FMH-Cl/NO_3-Hy has homogenously distributed cubic particles with an average particle size of approximately 100 nm, which could indicate the formation of α-FeOOH. FMH-Cl-Co showed an irregular morphology of stacked rods, while the FMH/FMO-NO_3-Co exhibited a bulk structure under SEM. However, upon calcination, the dimensions of the FMO-NO_3-Co particles were significantly reduced and as evidenced by TEM, there was a distinct transformation from bulk to lamellar structure.

The XRD pattern in Fig. 2a showed the crystalline state of FeMn-LDHs. The diffraction intensities at (012), (104), (110), (113), (202), and (018) crystalline lattice planes were found to be well-defined at 2θ = 24.2°, 31.4°, 37.5°, 41.4°, 45.1° and 51.5° [37]. It can be found that FeMn-LDH samples synthesized with nitrate exhibited significantly higher peak intensities than the ones with chloride, such as (012), (104), (018), indicating a better crystallinity. This observation suggests that the use of nitrate as a precursor promotes the crystal growth of FeMn-LDH more effectively. However, some impure peaks appeared in the spectrum from 15° to 20°, 25°–30° and 31.4°–37.5° of FMH-NO_3-Hy compared to FMH-NO_3-Co, which might be attributed to the formation of manganese oxides. The presence of water under elevated temperatures and pressures in the hydrothermal process can lead to the oxidation of Mn species [38]. In addition, there was a significant decrease in the crystallinity of the FMO-NO_3-Co, but all confirmed diffraction peaks have been preserved. Notably, the presence of numerous extraneous peaks suggests the potential formation of high-valence iron-manganese oxides [39].

Nitrogen adsorption and desorption isotherms (Fig. 2b) were applied to evaluate the specific surface area, total pore volume, and pore size distribution of LDHs. The FMO-NO_3-Co followed a type IV adsorption isotherm, and the corresponding hysteresis loops were H_3-type, meaning that it is a mesoporous material, according to the IUPAC standard. In comparison with the value of 10–17 m^2 g^{-1} prior to calcination, the SSA of FMO-NO_3-Co has witnessed an increase by several tens of times, attaining a value of 268.37 m^2 g^{-1}. The exponentially increasing SSA indicated that a greater number of reactive sites would be present on the calcined surface. Moreover, the pore size distribution curve reveals that the average pore size of FMO-NO_3-Co is 3.057 nm, and the existence of mesopores is conducive to the penetration of the electrolyte and the transportation of ions, thereby potentially accelerating the reaction kinetics.

The surface chemical states as well as electronic interactions of Fe and Mn were investigated with XPS. As shown in Fig. 2c and d, for all samples, the Fe 2p and Mn 2p spectra can be deconvoluted into two spin-orbit splitting peaks attributed to $2p_{1/2}$ and $2p_{3/2}$, and two (Fe) or one (Mn) satellite peaks (denoted as "sat."). In the case of FMH-Cl-Hy, for example, the two characteristic peaks at 710.9 eV and 723.6 eV were indexed to Fe^{2+} $2p_{3/2}$ and Fe^{2+} $2p_{1/2}$, respectively, while the peaks at 713.3 eV and 726.1 eV were indexed to Fe^{3+} $2p_{3/2}$ and Fe^{3+} $2p_{1/2}$, respectively. In addition, two accompanying satellite peaks were located at 717.9 eV and 730.7 eV. Thermal treatment at 400 °C exerted a neglectable effect on the valence state of Fe and the ratio of Fe^{2+}/Fe^{3+} was approximately 1:1. These results are reminiscent of the structure of magnetite (Fe_3O_4). Both valence states of iron are capable of specifically interacting with arsenic [40]. Similarly, Mn^{2+} 2p and Mn^{3+} 2p have been confirmed in the corresponding XPS patterns. Notably, upon calcination, the overall valence states of Mn increased, with the majority of Mn^{2+} being oxidized to Mn^{3+} and a minor fraction to Mn^{4+} (≈12 %). Concurrently, the distinctive satellite peaks associated with Mn^{2+} were nearly eliminated. The elevated valence states of Mn^{3+} and Mn^{4+} might contribute to the oxidation of As(III). However, the specific efficacy of these high-valence Mn species necessitates further experimental investigation.

The electrochemical performance of the electrodes was studied by CV and EIS. The specific capacitance (C_s) can be calculated as follows:

$$C_s = \frac{\int IdV}{2vm\Delta V} \quad (3)$$

where C_s is the specific capacitance (F g^{-1}), I is the response current (A), V is the potential (V), v is the potential scan rate (V s^{-1}). According to Fig. 3a, the values of specific capacitances of FMH-Cl-Hy, FMH-NO_3-Hy and FMH-Cl-Co were calculated to be 33.5 F g^{-1}, 22.5 F g^{-1} and 28.3 F g^{-1}, respectively, which were lower than that of FMH-NO_3-Co (54.68 F g^{-1}). The capacity was greatly improved after calcination (89.0 F g^{-1}), which can be attributed to the transition of the crystal

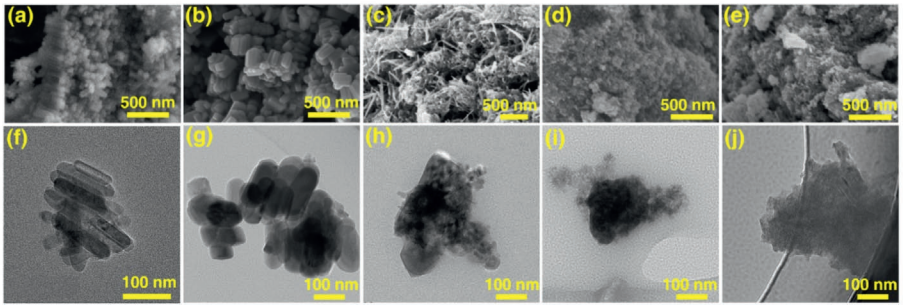

Fig. 1. SEM and TEM images of (a)(f) FMH-Cl-Hy, (b)(g) FMH-NO_3-Hy, (c)(h) FMH-Cl-Co, (d)(i) FMH-NO_3-Co and (e)(j) FMO-NO_3-Co.

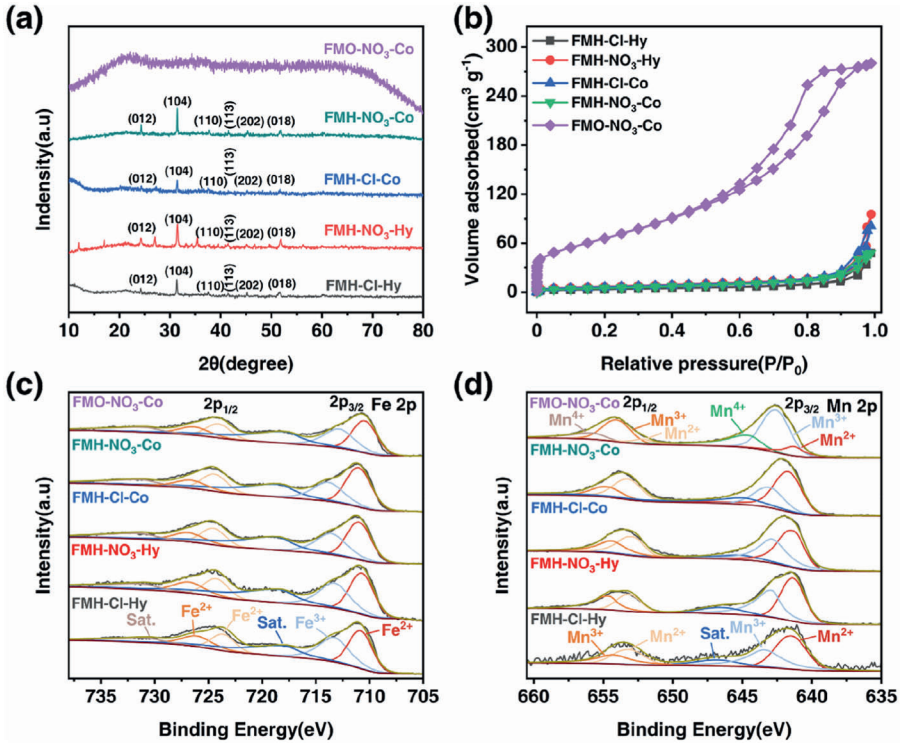

Fig. 2. (a) XRD patterns, (b) N_2 adsorption/desorption isotherms, (c) Fe 2p spectra, and (d) Mn 2p spectra of FMH-Cl-Hy, FMH-NO_3-Hy, FMH-Cl-Co, FMH-NO_3-Co and FMO-NO_3-Co.

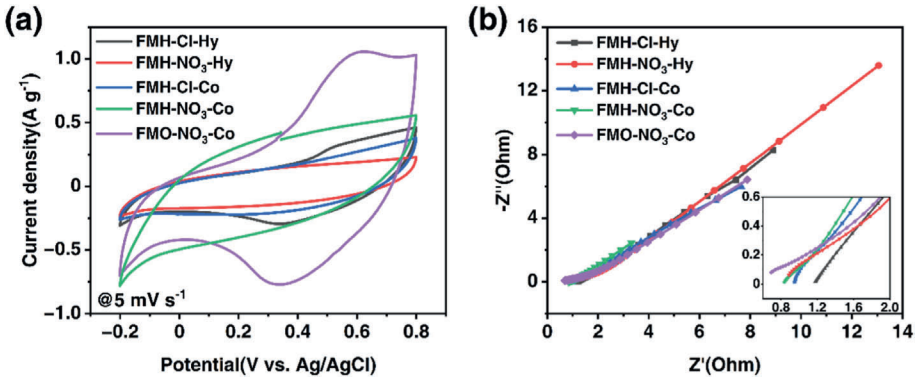

Fig. 3. (a) CV curves at a scan rate of 5 mV s^{-1} and (b) Nyquist plots of the FMH-Cl-Hy, FMH-NO_3-Hy, FMH-Cl-Co, FMH-NO_3-Co and FMH-NO_3-Co.

structure [39] and the oxidization of Mn(II) to Mn(III). The rapid reaction between Mn(II) and Mn(III) accelerates ion transfer and diffusion, thereby enhancing the capacitance. In Fig. 3b, the charge transfer resistance (R_{ct}) calculated from the EIS test was 1.16 Ω, 0.84 Ω and 0.93 Ω for the FMH-Hy-Cl, FMH-NO_3-Hy and FMH-Cl-Co, respectively. The FMH-NO_3-Co had smaller charge transfer resistance and a steeper linear gradient, indicating better electrochemical performance. The phase and structural transitions in FMO-NO_3-Co result in a lower charge transfer resistance.

Theoretically, the voltage is proportional to the charge on the electrodes. Therefore, as voltage increases, thicker EDL forms and more ions will be held. To minimize the influence of water electrolysis, we have established an electrosorption voltage of 1.2 V for a duration of 90 min (Step I). A constant cell voltage of −1.2 V for 90 min (Step II) was then applied to restore the electrode capacity for the next cycle. The corresponding anodic potential was 0.83 V vs SHE. Notably, the FMO-NO_3-Co electrode exhibited tunable redox potentials at 0.55/0.75 V vs SHE (Fig. 3a), corresponding to the redox reactions of Mn ($Mn^{2+} \leftrightarrow Mn^{3+}$). The higher redox potential of $Mn^{2+} \leftrightarrow Mn^{3+}$(The exact potential needs to be experimentally determined) would be beneficial to the oxidation of As(III) as follows [41].

$$H_3AsO_3+H_2O-2e^- \rightleftarrows HAsO_4^{2-}+4H^+ \; E = 0.56 \text{ V vs SHE} \quad (4)$$

The calcination process is known to induce an elevated valence state of Mn within FMO-NO_3-Co, a phenomenon confirmed by CV analysis. This increase in valence enhances their oxidation state and redox activity for the capture and conversion of trace arsenic in water.

Based on the above characterizations with insights for assessing arsenic remediation performance, two samples (FMH-NO_3-Co and FMO-NO_3-Co) excelled in stability, active-site quantity, and redox activity. We focused on these two for subsequent experiments in Fig. 4 highlighting their practical efficacy differences. Fig. 4a shows the removal of As(III) by using the FMH-NO_3-Co and FMO-NO_3-Co electrodes in a batch-mode CDI, in which the initial concentration of As(III) was 150 mg L^{-1}. The removal of arsenic reached 29.4 % and 51.4 % in 90 min with the As(III) sorption capacities of 37.5 and 55.5 mg g^{-1} at

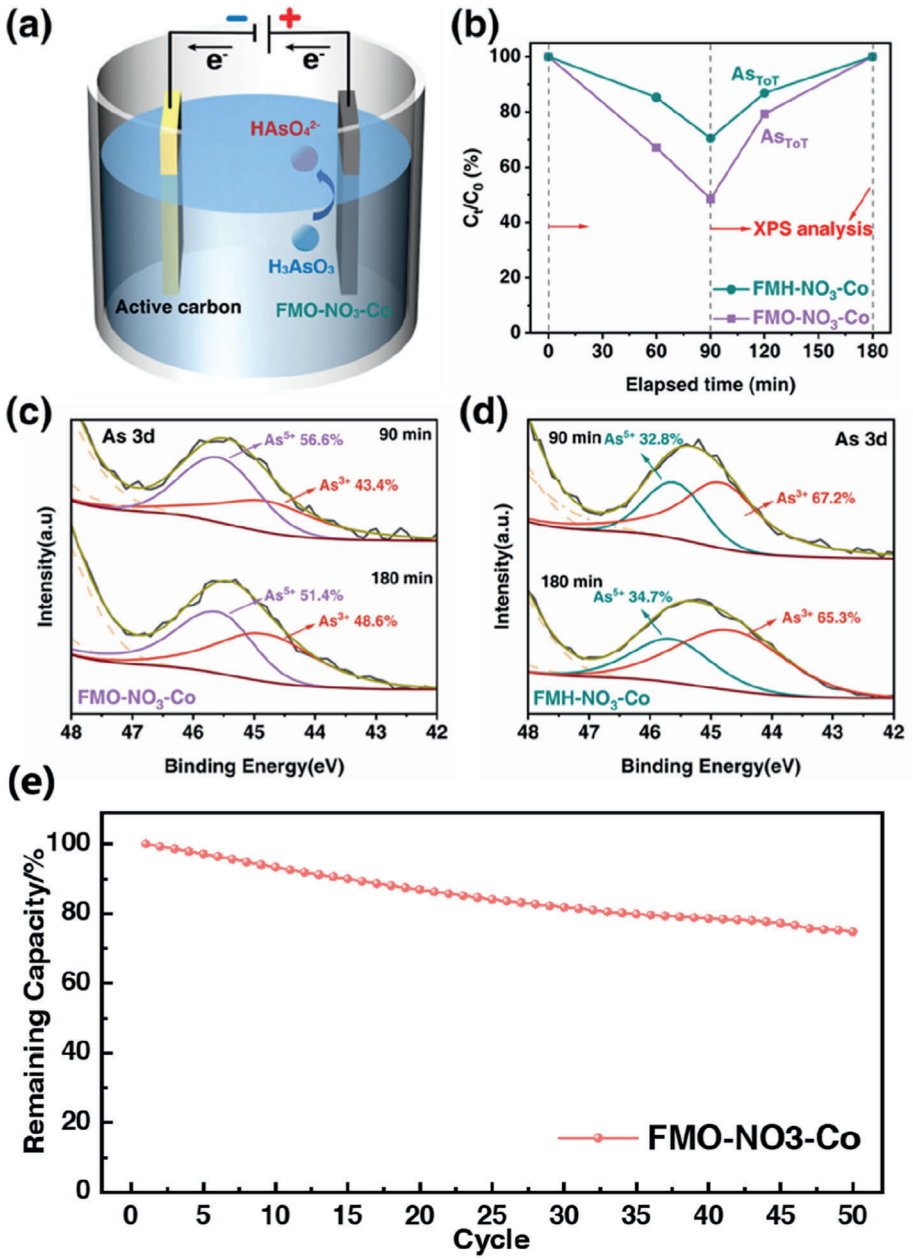

Fig. 4. (a) Illustration of the electrochemical system, (b) Changes in the total arsenic concentrations (As_{TOT}) in a cycle using FMH-NO_3-Co and FMO-NO_3-Co as working electrodes. High-resolution As 3d spectra of (c) FMO-NO_3-Co and (d) FMH-NO_3-Co electrodes at 90 min and 180 min, (e) Capacity retention of the FMO-NO_3-Co electrode over 50 charge/discharge cycles.

1.2 V, respectively. After a duration of 90 min reversed polarity, the arsenic concentration within the solution nearly returned to the initial level. To understand the mechanisms behind the electrocatalytic conversion of As(III) to As(V), XPS analysis was carried out on the FMH-NO_3-Co and FMO-NO_3-Co (working electrodes) in the pristine (at the 0 min), end of the Step I (at the 90 min) and Step II (at the 180 min) (Fig. 4c and d). During the charging process at 1.2 V, oxidation of As(III) was observed at Step I. High-resolution As 3d spectra demonstrated that the adsorbed As(III) on FMO-NO_3-Co was significantly converted into As (V) (56.6 %). In contrast, As(III) was the dominant species on the positively charged FMH-NO_3-Co with only 32.8 % of As(III) converted into As(V). This may be due to the fact that most of As(III) ions in the solution were oxidized to As (V) with the presence of high valence manganese, after which As (V) was fixed on the anode. Additionally, the capacity retention of the FMO-NO_3-Co electrode was evaluated over 50 charge/discharge cycles between −0.2 V and 0.8 V (Fig. 4e). After 50 cycles, 74.8 % of the initial capacity was retained, indicating superior cycling stability.

To better determine the mechanism of As conversion, the XPS spectral peaks of O 1s, Fe 2p, and Mn 2p were analyzed, especially comparing the changes before and after charging (beginning and end of Step I). As shown in Fig. 5, the high-resolution XPS analysis provided insights into the chemical environment and oxidation states. As for the pristine FMH-NO_3-Co, the spectrum of O 1s can be deconvoluted into three peaks with binding energies of 530.0, 531.5 and 532.8 eV, representing surface lattice oxygen, surface hydroxyl and adsorbed oxygen, respectively [39]. Similarly, for FMO-NO_3-Co, the O1s spectral peaks exhibit significant broadening subsequent to heat treatment. Moreover, as for FMO-NO_3-Co, the percentage of Fe-O groups decreased from 46.3 % to 44.1 % and 38 % in the O 1s high-resolution spectra, which followed the same trend for FMH-NO_3-Co. This phenomenon was ample evidence that adsorption was based on the substitution of Fe-OH groups

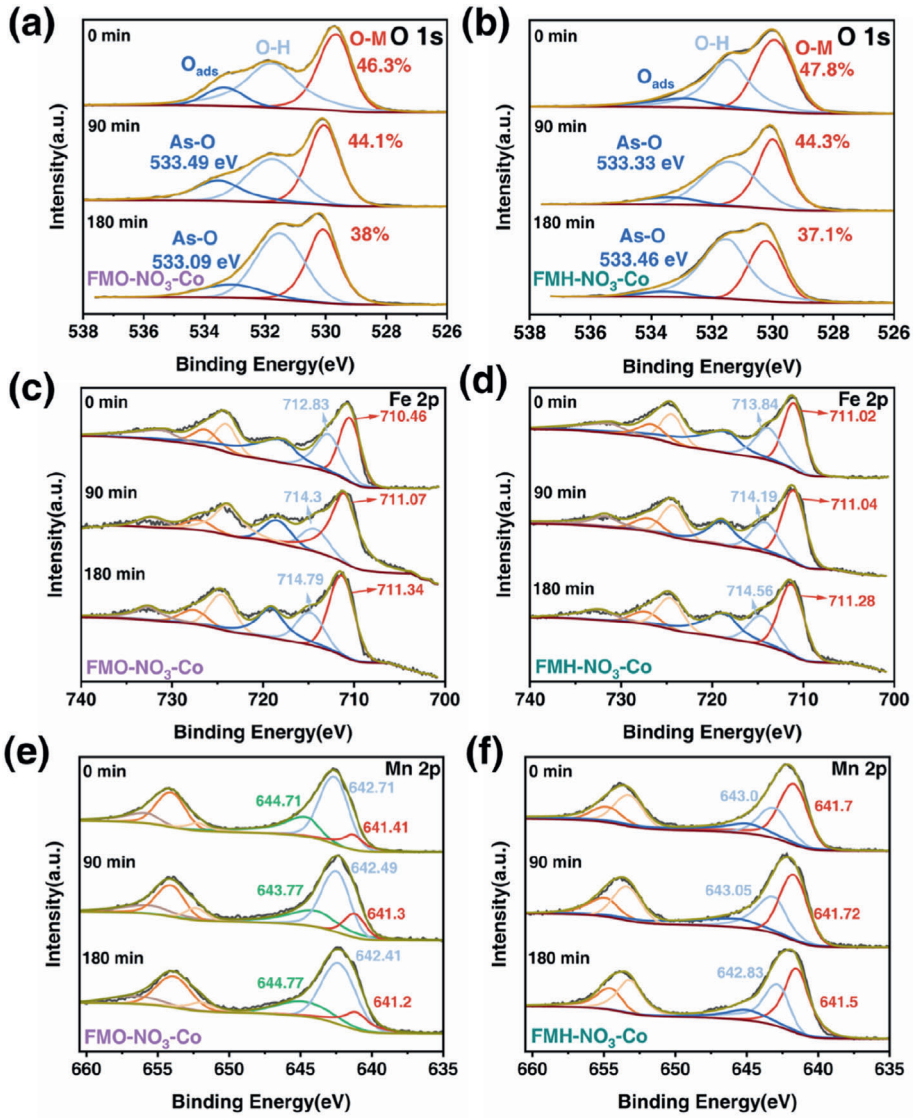

Fig. 5. (a) (b) O 1s, (c) (d) Fe 2p and (e) (f) Mn 2p spectra of FMO-NO_3-Co and FMH-NO_3-Co, respectively, at the 0 min, 90 min and 180 min.

by arsenic [42]. Moreover, a relatively substantial alteration in the proportion of surface hydroxyl groups was also detected. This finding implied that these surface hydroxyl groups were, to some extent, engaged in the adsorption process of As[25]. Furthermore, the binding energies of Fe 2p spectra shifted to a higher region after As(III) adsorption, resulting from the chemical interaction of iron and arsenic and the formation of Fe-O-As bond during adsorption [43,44]. At last, the binding energies of FMO-NO_3-Co and FMH-NO_3-Co shifted to a lower level after As(III) adsorption, which can be elucidated by the increase in the proportion of reduced Mn species relative to Mn(III). Nesbitt et al. also analyzed the Mn 2p spectra before and after its reaction with As(III) showing that the binding energies of Mn(IV), Mn(III), and Mn(II) species were in the low-energy side [45].

Based on the above results, it can be concluded that the efficient adsorption of As stems from the synergistic combination of electrostatic and chemical coordination. As(III) is difficult to capture directly. As shown in Fig. 6, part of the adsorbed As(III) is stored in the electrical double layer (EDL), while the rest is oxidized to As(V) by a small amount of Mn^{3+} at approximately 0.7 V. As(V) is more readily captured by the anode, where it is partially stored in the EDL and partially coordinated with the Fe oxides. Upon the reverse of the applied voltage (Step II), the absorbed arsenic is desorbed, accompanied by the reduction of Mn^{3+} to

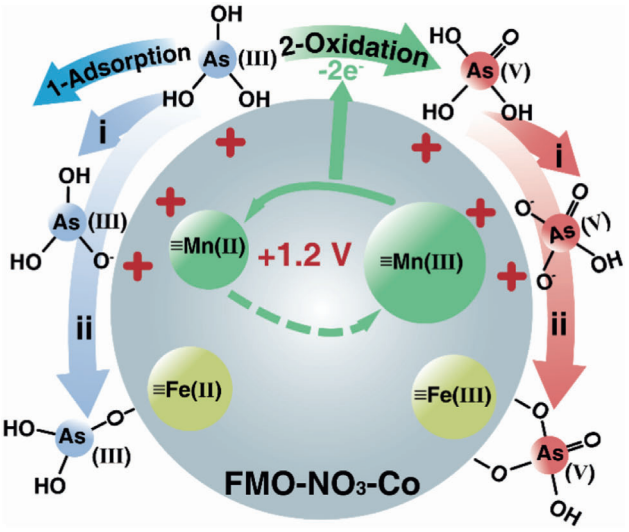

Fig. 6. The As (V) and As (III) removal mechanism on the FMO-NO_3-Co/AC electrode.

Table 1
Comparison of this work with previously reported studies.

	This article	[46]	[47]	[48]	[49]
Conversion rate/%	56.6	62	60	85	51.5 ± 1.3
Arsenic adsorption capacity	55.5 mg g^{-1}	93.15 mg g^{-1}	48 mg g^{-1}	0.495 mg g^{-1}	46.35 μg g^{-1}

Mn^{2+}, preparing the system for the next cycle. The rapid reaction between Mn^{3+} and Mn^{2+} facilitates the overall cycling process. Calcination treatment effectively enhances the oxidation state of Mn species, removes adsorbed water, and increases the density of surface hydroxyl groups, thereby accelerating the arsenic adsorption and conversion processes throughout the entire removal cycle, leading to more efficient arsenic removal. Furthermore, we compared the present study with other arsenic-removal works (Table 1). In high-concentration solutions, the FMO-NO_3-Co electrode delivers competitive adsorption capacity and arsenic conversion efficiency.

4. Conclusions

In this work, we highlight the potential of FeMn-LDH as a promising material for electrochemical arsenic removal. By employing hydrothermal and co-precipitation methods, we successfully synthesized FeMn-LDH with enhanced crystallinity when using nitrate precursors. The calcination process further improved its specific surface area and pore size, leading to superior ion transport and reaction kinetics. Electrochemical analysis revealed that FMO-NO_3-Co exhibited excellent specific capacitance and electrocatalytic activity, particularly in the oxidation of As(III). The electrode achieved an electrosorption capacity of 55.5 mg g^{-1} through in-situ oxidation of As(III) to As(V) and subsequent electrosorption. The superior performance was attributed to multiple synergistic factors: (1) the Mn^{2+}/Mn^{3+} redox couple facilitated As(III) oxidation, (2) the Fe sites provided strong coordination with As (V), ensuring high adsorption efficiency, and (3) the enhanced conductivity and porous structure improved charge transfer and ion diffusion, leading to accelerated arsenic removal. These findings highlight the importance of structural and chemical modifications in optimizing LDH-derived materials for electrochemical water treatment. This study provides new insights into the design of multifunctional electrode materials, offering a promising strategy for sustainable and efficient electrochemical remediation of arsenic-contaminated water.

CRediT authorship contribution statement

Song Peng: Writing – original draft, Methodology, Investigation. **Tiantian Wang:** Validation. **Yang Wang:** Writing – review & editing, Supervision, Project administration, Funding acquisition.

Declaration of competing interest

The authors declare that they have no known competing financial interests or personal relationships that could have appeared to influence the work reported in this paper.

Acknowledgment

This work was supported by the National Natural Science Foundation of China (No.22178253) and the Tianjin Metrology Technology Project (No. 2024TJMT038).

References

[1] J.F. Ferguson, J. Gavis, A review of the arsenic cycle in natural waters, Water Res. 6 (11) (1972) 1259–1274, https://doi.org/10.1016/0043-1354(72)90052-8.
[2] Y. Wang, J. Yu, Z. Wang, Y. Liu, Y. Zhao, A review on arsenic removal from coal combustion: advances, challenges and opportunities, Chem. Eng. J. 414 (2021) 128785, https://doi.org/10.1016/j.cej.2021.128785.
[3] B.S. Rathi, P.S. Kumar, A review on sources, identification and treatment strategies for the removal of toxic arsenic from water system, J. Hazard. Mater. 418 (2021) 126299, https://doi.org/10.1016/j.jhazmat.2021.126299.
[4] A. Duker, E. Carranza, M. Hale, Arsenic geochemistry and health, Environ. Int. 31 (5) (2005) 631–641, https://doi.org/10.1016/j.envint.2004.10.020.
[5] M.M. Rahman, J.C. Ng, R. Naidu, Chronic exposure of arsenic via drinking water and its adverse health impacts on humans, Environ. Geochem. Health 31 (S1) (2009) 189–200, https://doi.org/10.1007/s10653-008-9235-0.
[6] T.S.Y. Choong, T.G. Chuah, Y. Robiah, F.L. Gregory Koay, I. Azni, Arsenic toxicity, health hazards and removal techniques from water: an overview, Desalination 217 (1–3) (2007) 139–166, https://doi.org/10.1016/j.desal.2007.01.015.
[7] D. Anh Nguyen, D. Viet Nguyen, G. Jeong, N. Asghar, A. Jang, Critical evaluation of hybrid metal–organic framework composites for efficient treatment of arsenic–contaminated solutions by adsorption and membrane–separation process, Chem. Eng. J. 461 (2023) 141789, https://doi.org/10.1016/j.cej.2023.141789.
[8] K. Banerjee, R.P. Helwick, S. Gupta, A treatment process for removal of mixed inorganic and organic arsenic species from groundwater, Environ. Prog. 18 (4) (1999) 280–284, https://doi.org/10.1002/ep.670180415.
[9] E.F. Zama, G. Li, Y.-T. Tang, B.J. Reid, N.M. Ngwabie, G.-X. Sun, The removal of arsenic from solution through biochar-enhanced precipitation of calcium-arsenic derivatives, Environ. Pollut. 292 (2022) 118241, https://doi.org/10.1016/j.envpol.2021.118241.
[10] A.S. Chevinli, J. Rahmatinejad, N. Hmidi, D. Rodrigue, Z. Ye, Mg Fe layered double hydroxide-graphene oxide nanocomposite adsorbents for arsenic removal, J. Water Process Eng. 59 (2024) 105017, https://doi.org/10.1016/j.jwpe.2024.105017.
[11] H. Yu, J. Li, W. Qu, W. Wang, J. Wang, High-efficiency removal of as(iii) from groundwater using siderite as the iron source in the electrocoagulation process, RSC Adv. 14 (27) (2024) 19206–19218, https://doi.org/10.1039/D4RA02716G.
[12] P. Li, J.T. Damron, G.M. Veith, V.S. Bryantsev, S.M. Mahurin, I. Popovs, S. Jansone-Popova, Bifunctional ionic covalent organic networks for enhanced simultaneous removal of Chromium(VI) and Arsenic(V) oxoanions via synergetic ion exchange and redox process, Small 17 (46) (2021) 2104703, https://doi.org/10.1002/smll.202104703.
[13] M.E. Suss, S. Porada, X. Sun, P.M. Biesheuvel, J. Yoon, V. Presser, Water desalination via capacitive deionization: what is it and what can we expect from it? Energy Environ. Sci. 8 (8) (2015) 2296–2319, https://doi.org/10.1039/C5EE00519A.
[14] Y.-W. Chen, J.-F. Chen, C.-H. Lin, C.-H. Hou, Integrating a supercapacitor with capacitive deionization for direct energy recovery from the desalination of brackish water, Appl. Energy 252 (2019) 113417, https://doi.org/10.1016/j.apenergy.2019.113417.
[15] L. Luo, T. Liu, J. He, J. Ma, H.-Q. Yu, Interface gypsum deposition in flow-electrode CDI treating brackish water: impacts and mechanisms, Water Res. 272 (2025) 122920, https://doi.org/10.1016/j.watres.2024.122920.
[16] S. Sahin, J.E. Dykstra, H. Zuilhof, R.L. Zornitta, L.C.P.M. De Smet, Modification of cation-exchange membranes with polyelectrolyte multilayers to tune ion selectivity in capacitive deionization, ACS Appl. Mater. Interfaces 12 (31) (2020) 34746–34754, https://doi.org/10.1021/acsami.0c05664.
[17] A. Tripathi, S. Dahiya, B.K. Mishra, Next-generation heavy metal water treatment: a primer on modified capacitive deionization, Chem. Eng. J. 505 (2025) 158844, https://doi.org/10.1016/j.cej.2024.158844.
[18] X. Liu, D. Rehman, Y. Shu, B. Liu, L. Wang, L. Li, M. Wang, K. Wang, Q. Han, L. Zang, J.H. Lienhard, Z. Wang, Selective fluoride removal from groundwater using CNT-CeO2 electrodes in capacitive deionization (CDI), Chem. Eng. J. 482 (2024) 149097, https://doi.org/10.1016/j.cej.2024.149097.
[19] M. Askari, S. Rajabzadeh, L. Tijing, H.K. Shon, Advances in capacitive deionization (CDI) systems for nutrient recovery from wastewater: paving the path towards a circular economy, Desalination 583 (2024) 117695, https://doi.org/10.1016/j.desal.2024.117695.
[20] S. Bao, C. Xin, Y. Zhang, B. Chen, W. Ding, Y. Luo, Application of capacitive deionization in water treatment and energy recovery: a review, Energies 16 (3) (2023) 1136, https://doi.org/10.3390/en16031136.
[21] P.-C. Wu, D. Viet Cuong, J.-C. Wu, S. Ya Hsuan Liou, C.-H. Hou, Harnessing In-Situ electrocatalytic oxidation with a cobalt oxide decorated nanocomposite electrode for efficient arsenic removal in capacitive deionization, Chem. Eng. J. 474 (2023) 145887, https://doi.org/10.1016/j.cej.2023.145887.
[22] Y.-J. Shih, Z.-S. Chen, C.-L. Chen, Y.-H. Huang, C.-P. Huang, Enhancing arsenic (III) removal by integrated electrocatalytic oxidation and electrosorption reactions on nano-textured bimetal composite of iron oxyhydroxide and manganese dioxide polymorphs (α-, γ-, β-, and ε-MnxFe1−xO), Appl. Catal., B 317 (2022) 121757, https://doi.org/10.1016/j.apcatb.2022.121757.
[23] Y. Zhang, Y. Deng, J. Xue, Y. Cheng, Y. Nie, K. Pi, Y. Du, X. Xie, J. Shi, Y. Wang, Unravelling the impacts of soluble Mn(III)-NOM on arsenic immobilization by ferrihydrite or goethite under aquifer conditions, J. Hazard. Mater. 466 (2024) 133640, https://doi.org/10.1016/j.jhazmat.2024.133640.
[24] J. Ai, W.H.M. Abdelraheem, S. Peng, W. Guo, X. Duan, S. Peng, W. Zhang, Q. Wang, D.D. Dionysiou, AsIII-Enhanced oxidation by coexisting MnIII-Phenolic complexes

during arsenic contaminated groundwater treatment by MnO2, Sep. Purif. Technol. 344 (2024) 127254, https://doi.org/10.1016/j.seppur.2024.127254.
[25] L. Cai, B. Xu, Y. Gan, Y. Liu, Z. Chen, W. Yang, J. Zhang, K. Jiang, Effective removal of trace arsenic from groundwater by capacitive deionization, Sep. Purif. Technol. 330 (2024) 125419, https://doi.org/10.1016/j.seppur.2023.125419.
[26] L. Yang, S. Liu, H. Zhang, W. Zhang, W. Ding, H. Zheng, H. Li, J. Zhai, Insight into the purification of arsenic-contaminated acid water by metal–organic framework MIL-53(Fe) with sulfite: the generation and effect of Fe(IV), Chem. Eng. J. 481 (2024) 148766, https://doi.org/10.1016/j.cej.2024.148766.
[27] Y. Yuan, X. Wei, M. Zhu, Y. Cai, Y. Wang, Z. Dang, H. Yin, Unravelling the removal mechanisms of trivalent arsenic by sulfidated nanoscale zero-valent iron: the crucial role of reactive oxygen species and the multiple effects of citric acid, Sci. Total Environ. 916 (2024) 170275, https://doi.org/10.1016/j.scitotenv.2024.170275.
[28] Z. Wen, J. Lu, Y. Zhang, G. Cheng, S. Guo, P. Wei, Y. Ming, Y. Wang, R. Chen, Simultaneous oxidation and immobilization of arsenite from water by nanosized magnetic mesoporous iron manganese bimetal oxides (Nanosized-MMIM): synergistic effect and interface catalysis, Chem. Eng. J. 391 (2020) 123578, https://doi.org/10.1016/j.cej.2019.123578.
[29] S. Peng, Q. Pan, Y. Qiao, T. Wang, N.L. Htut, B. Chen, M.A. Anderson, Y. Wang, J. Qiu, Importance of morphology of layered double hydroxide in electrochemical energy storage and catalysis, Small Methods (2024) 2400519, https://doi.org/10.1002/smtd.202400519.
[30] Y. Wang, Q. Pan, Y. Qiao, X. Wang, D. Deng, F. Zheng, B. Chen, J. Qiu, Layered metal oxide nanosheets with enhanced interlayer space for electrochemical deionization, Adv. Mater. (2023) 2210871, https://doi.org/10.1002/adma.202210871.
[31] Y. Qiao, Y. Li, C. Wang, Q. Pan, B. Chen, Y. Wang, Layered double oxide as a cl−selective anode for high-performance electrochemical lithium extraction, ACS Sustainable Chem. Eng. 12 (31) (2024) 11692–11704, https://doi.org/10.1021/acssuschemeng.4c03437.
[32] Y. Qiao, Y. Li, Y. Wang, J. Qiu, Layered double hydroxide for electrochemical ion separation, Desalination 596 (2025) 118353, https://doi.org/10.1016/j.desal.2024.118353.
[33] Y. Zhang, S. Hu, C. Li, X. Yan, Y. Zhang, R. Yin, Y. Wei, K. Gao, H. Gao, Advanced strategies for enhancing electrochemical performance of NiAl LDH electrodes in supercapacitors, Coord. Chem. Rev. 531 (2025) 216497, https://doi.org/10.1016/j.ccr.2025.216497.
[34] Y. Zhang, C. Zhou, X. Yan, Y. Cao, H. Gao, H. Luo, K. Gao, S. Xue, X. Jing, Recent advances and perspectives on graphene-based gels for superior flexible all-solid-state supercapacitors, J. Power Sources 565 (2023) 232916, https://doi.org/10.1016/j.jpowsour.2023.232916.
[35] Y. Zhang, C.-G. Zhou, X. Yan, H.-L. Gao, K.-Z. Gao, Y. Cao, Synthesis of nafion-reduced graphene oxide/polyaniline as novel positive electrode additives for high performance lead-acid batteries, Electrochim. Acta 466 (2023) 143045, https://doi.org/10.1016/j.electacta.2023.143045.
[36] Y. Zhang, Y. Wei, X. Jing, Z. Fan, S. Hu, Y. Zhang, R. Yin, H. Gao, One-step synthesis of nano-onion-like NiCoMn-LDHs for high-performance supercapacitors, Int. J. Appl. Ceram. Technol. 22 (4) (2025) e15138, https://doi.org/10.1111/ijac.15138.
[37] E. Otgonjargal, Y.-S. Kim, S.-M. Park, K. Baek, S. Yang, Mn–Fe layered double hydroxides for adsorption of As(III) and As(V), Separ. Sci. Technol. 47 (14–15) (2012) 2192–2198.
[38] M. Musil, B. Choi, A. Tsutsumi, Morphology and electrochemical properties of α-, β-, γ-, and δ-MnO2 synthesized by redox method, J. Electrochem. Soc. 162 (10) (2015) A2058–A2065, https://doi.org/10.1149/2.0201510jes.
[39] X. Zhou, Y. Wang, X. Wang, Y. Zhang, Successful fabrication of iron-manganese (Fe-Mn) layered double bimetallic oxide for the degradation of sulfathiazole via peroxymonosulfate activation: performance, degradation mechanism and pathway, J. Environ. Chem. Eng. 11 (3) (2023) 110120, https://doi.org/10.1016/j.jece.2023.110120.
[40] C.-H. Liu, Y.-H. Chuang, T.-Y. Chen, Y. Tian, H. Li, M.-K. Wang, W. Zhang, Mechanism of arsenic adsorption on magnetite nanoparticles from water: thermodynamic and spectroscopic studies, Environ. Sci. Technol. 49 (13) (2015) 7726–7734, https://doi.org/10.1021/acs.est.5b00381.
[41] P. Vanýsek, Electrochemical Series. Handbook of Chemistry and Physics, CRC Press, 2012, pp. 5–18.
[42] D.V. Cuong, P.-C. Wu, L.-I. Chen, C.-H. Hou, Active MnO2/Biochar composite for efficient As(III) removal: insight into the mechanisms of redox transformation and adsorption, Water Res. 188 (2021) 116495, https://doi.org/10.1016/j.watres.2020.116495.
[43] D. Fu, Z. He, S. Su, B. Xu, Y. Liu, Y. Zhao, Fabrication of α-FeOOH decorated graphene oxide-carbon nanotubes aerogel and its application in adsorption of arsenic species, J. Colloid Interface Sci. 505 (2017) 105–114, https://doi.org/10.1016/j.jcis.2017.05.091.
[44] X. Ge, Y. Ma, X. Song, G. Wang, H. Zhang, Y. Zhang, H. Zhao, β-FeOOH nanorods/carbon foam-based hierarchically porous monolith for highly effective arsenic removal, ACS Appl. Mater. Interfaces 9 (15) (2017) 13480–13490, https://doi.org/10.1021/acsami.7b01275.
[45] H.W. Nesbitt, G.W. Canning, G.M. Bancroft, XPS study of reductive dissolution of 7Å-Birnessite by H3AsO3, with constraints on reaction mechanism, Geochem. Cosmochim. Acta 62 (12) (1998) 2097–2110, https://doi.org/10.1016/S0016-7037(98)00146-X.
[46] K. Bisaria, S. Sinha, H.M.N. Iqbal, R. Singh, Ultrasonication expedited As(III) adsorption onto chitosan impregnated Ni–Fe layered double hydroxide biosorbent: optimization studies and artificial intelligence modelling, Environ. Res. 212 (2022) 113184, https://doi.org/10.1016/j.envres.2022.113184.
[47] Y.-J. Shih, Z.-S. Chen, C.-L. Chen, Y.-H. Huang, C.-P. Huang, Enhancing arsenic (III) removal by integrated electrocatalytic oxidation and electrosorption reactions on nano-textured bimetal composite of iron oxyhydroxide and manganese dioxide polymorphs (α-, γ-, β-, and ε-MnxFe1−xO), Appl. Catal. B Environ. 317 (2022) 121757, https://doi.org/10.1016/j.apcatb.2022.121757.
[48] L. Cai, B. Xu, Y. Gan, Y. Liu, Z. Chen, W. Yang, J. Zhang, K. Jiang, Effective removal of trace arsenic from groundwater by capacitive deionization, Separ. Purif. Technol. 330 (2024) 125419, https://doi.org/10.1016/j.seppur.2023.125419.
[49] Z. Song, S. Garg, J. Ma, T.D. Waite, Selective arsenic removal from groundwaters using redox-active Polyvinylferrocene-Functionalized electrodes: role of oxygen, Environ. Sci. Technol. 54 (19) (2020) 12081–12091, https://doi.org/10.1021/acs.est.0c03007.